ACS NANO

www.acsnano.org

ARTICLE

Phase Changes of Multielemental Alloy Nanoparticles at Elevated Temperatures

Zhennan Huang,[▽] Tangyuan Li,[▽] Ying Fang,[▽] Jacob Smith, Boyang Li, Alexandra Brozena, Qi Dong, Qian Zhang, Yiheng Du, Scott X. Mao, Guofeng Wang,* Miaofang Chi,* and Liangbing Hu*

Cite This: *ACS Nano* 2025, 19, 13457−13465

Read Online

ACCESS | Metrics & More | Article Recommendations | Supporting Information

ABSTRACT: **Multielemental alloy (MEA) nanomaterials, such as medium and high entropy alloys, display promising catalytic performance in a range of chemical reactions due to their multicomponent structural configurations. These complex structural and chemical arrangements can be influenced by several factors, such as mechanical stress, irradiation, and high temperatures, which impact the performance of MEAs in various applications. Here, we investigated the effect of high temperatures on MEA nanoparticles composed of noble and transition metals (quaternary PtPdFeCo) at the atomic scale and found the material undergoes a series of phase transitions between solid solution and intermetallic phases at elevated temperatures ranging from room temperature to 1073 K. In contrast, the binary PtFe nanoalloy displays a one-way solid solution to intermetallic transition at these temperatures. Our findings, rationalized by density functional theory (DFT) studies, demonstrate how the varied migration energies of elements govern the solid solution to intermetallic transition and how differences in the bonding energies of elemental pairs influence the Gibbs free energy change (ΔG), which dictates the intermetallic to solid-solution transition. Overall, this work provides better guidance in the design, development, and usage of nano-MEAs for high-temperature-based applications.**

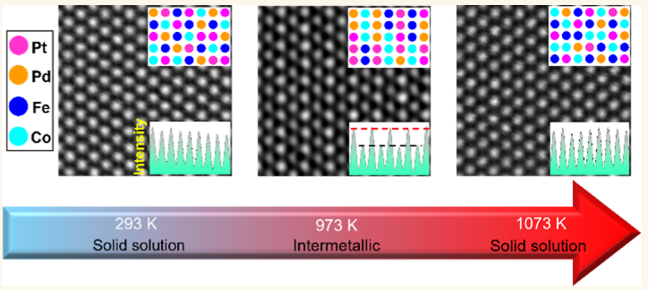

KEYWORDS: *multielemental alloy, thermal stability, phase evolution, solid solution, intermetallic structure*

Multielemental alloys (MEAs), such as medium and high entropy alloys, constitute a novel class of complex materials that are formed by combining multiple elements into a solid-solution structure, exhibiting remarkable properties across a wide spectrum of applications.[1−7] With efficient integration of broad elemental combinations, including high value noble and rare earth transition metals as primary constituents, nanostructured MEAs have emerged as a new materials design strategy[8] for applications in energy storage/conversion and catalysis,[8−15] combining tunable compositional design,[16−18] synergistic effects between neighboring elemental atoms,[19] and enhanced durability against harsh environments.[20−22] However, some conditions, such as strain[23−25] and elevated temperatures,[26] can promote the formation of secondary or intermetallic phases from the original MEA solid-solution structure.[26−28] In particular, nano-MEAs combining noble and transition metals can become more ordered, trending toward intermetallic phases at high temperatures.[29,30] This phase transformation reduces the compositional randomness and elemental synergy within the alloy, leading to variable performance under working conditions.[31,32] For example, high-entropy intermetallic catalysts exhibit varied selectivity for alkyne semihydrogenation compared to less-ordered structures.[33] Intermetallic nanocrystals also play large roles in fuel-cell,[34] alcohol oxidation,[35] and other chemical reactions,[36] while their disordered counterparts do not display strong performance for these reactions.[37] In contrast, the synergistic effect of multiple elementals in solid solution alloys has been shown to enable superior performance on enzymatic catalysis,[38] ammonium chemistry,[9,39] and hydrogen reactions.[40] Therefore, it is essential to understand these phase transitions to better design, control, and utilize nano-MEAs under common catalytic conditions.

However, our understanding of this phase transformation process is fairly limited due to the complexity of the multielemental mixing, featuring a combination of randomly distributed elements and small localized features (e.g., distortions,[41] short-range ordering,[42,43] secondary phases,[44,45]

Received: February 8, 2025
Revised: March 17, 2025
Accepted: March 18, 2025
Published: March 26, 2025

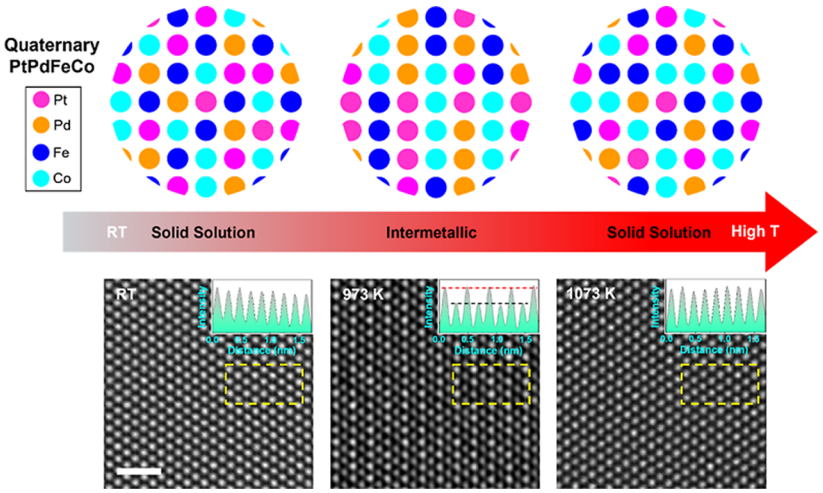

Figure 1. Phase transformations in PtPdFeCo-MEA NPs at elevated temperatures. The PtPdFeCo alloy demonstrates phase transformations from solid solution to intermetallic and back to solid solution again as the temperature increases from room temperature (RT) to 973 K and subsequently 1073 K, as demonstrated by the atomic HAADF-STEM images and corresponding intensity line profiles (dashed regions) showing the change in Z contrast at each stage of heating. Scale bar 1 nm.

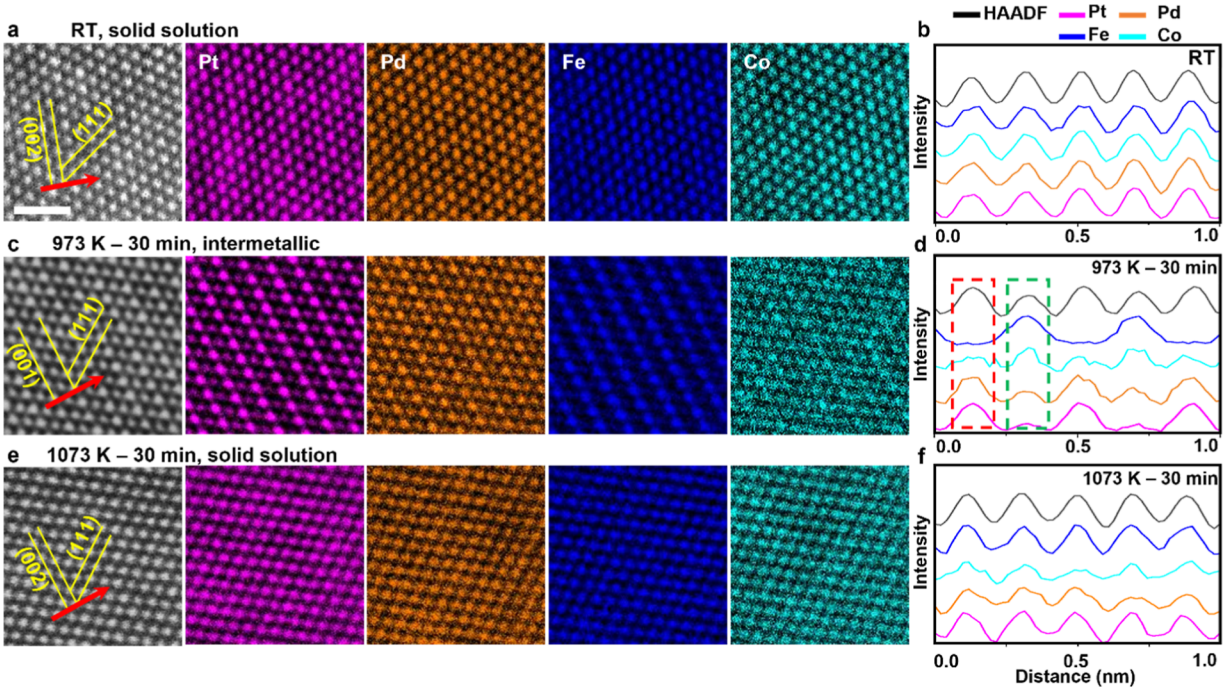

Figure 2. Structural and chemical changes of PtPdFeCo NPs at elevated temperatures. HAADF-STEM, STEM-EDS mapping, and line scan analysis of a PtPdFeCo-MEA NP at (a,b) room temperature, (c,d) after heating at 973 K for 30 min, and (e,f) further heating at 1073 K for 30 min (scale bar 1 nm). The corresponding EDS line scan profile analyses are along the direction (red arrow in HAADF images) perpendicular to the (001)/(002) planes. The PtPdFeCo alloy features a solid solution alloy structure at room temperature that transforms into an intermetallic phase of $L1_0$ (PtPd)(FeCo) after heating at 973 K for 30 min and then back to a solid-solution structure when further heated at 1073 K for 30 min.

etc.). Greater understanding of how temperature influences noble-transition metal nano-MEAs at the atomic level, both structurally and chemically, is needed to better control the mechanism and driving forces behind any phase changes and thus enable better design and utilization of these nanomaterials for high-temperature pretreatment or advanced high-temperature applications.

Herein, we explore the dynamic transformation of a noble-transition-metal MEA at elevated temperature using a combination of structural and elemental analyses with real-time atomic-scale capabilities. For these studies, we synthesized and investigated quaternary MEA nanoparticles (NPs) composed of noble metal elements (Pt and Pd) in combination with transition metals (Fe and Co), which are extensively used in high-temperature catalytic applications.[46−52] During in situ heating, the evolution of the PtPdFeCo-MEA NPs was systematically monitored for any structural and elemental transformations using scanning transmission electron microscopy (STEM) with high angle annular dark field (HAADF) imaging, as well as high-resolution energy dispersive X-ray

https://doi.org/10.1021/acsnano.5c02343
ACS Nano 2025, 19, 13457−13465

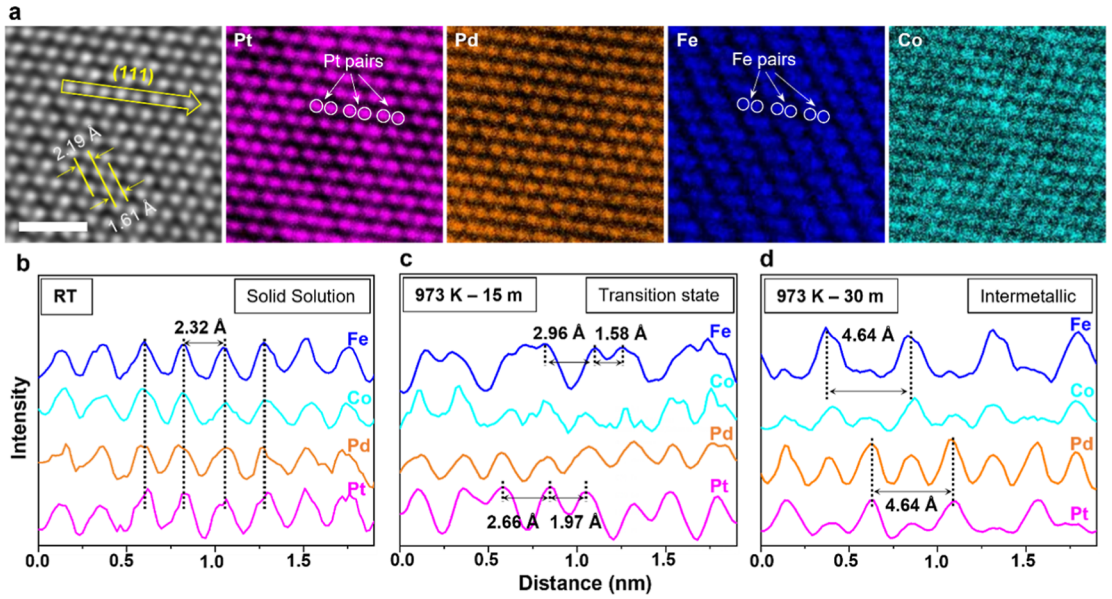

Figure 3. (a) Atomic-STEM image and corresponding elemental maps of Pt, Pd, Fe, and Co after the 973 K-15 min heat treatment. (b–d) EDS line profiles along the atomic columns on the (111) planes (yellow arrow) of the PtPdFeCo alloy at (b) RT, (c) after the 973 K-15 min, and (d) 973 K-30 min heat treatment. (scale bar 1 nm).

spectroscopy (EDS). Our findings reveal a disorder-to-order phase transition that occurs within the PtPdFeCo NPs upon heating to 973 K, which triggers the migration and ordering of the elements, particularly Pt and Fe, leading to the formation of an intermetallic $L1_0$ (PtPd)(FeCo) species. After further heating to 1073 K, the quaternary intermetallic compound transforms back to a disordered solid-solution phase, regaining the original structure, as shown in Figure 1. For comparison, we also synthesized a binary PtFe solid solution alloy and found it displayed a straightforward transition to an intermetallic structure at similar temperatures. Density functional theory (DFT) calculations indicate that during the disorder-to-order transition, the relatively low migration energies of Pt and Fe play a critical role in driving the migration and ordering of the elements into intermetallic sublattices. In contrast, the order-to–disorder transition takes place only in the (PtPd)(FeCo) intermetallic, primarily due to its lower change in bonding energies (ΔE), facilitating easier bond reconstruction, which reduces the Gibbs free energy change (ΔG) for the phase transformation compared to PtFe, thus enabling phase transition at a lower temperature. The high-temperature phase transitions of this noble-transition-metal PtPdFeCo-MEA can help us to better understand the driving forces taking place during phase transition and how they may impact similar MEA nanomaterials, which could provide better guidance for maintaining the functionality of MEAs during high-temperature applications.

RESULTS AND DISCUSSION

We synthesized the quaternary PtPdFeCo NPs using a nonequilibrium carbothermal shock method, which involves fast temperature quenching during the high-temperature synthesis to kinetically trap the solid solution structure at room temperature.[1] HAADF-STEM imaging indicated the NPs were ~20 nm in size, with the corresponding STEM-EDS maps showing the Pt, Pd, Fe, and Co signals are well distributed throughout the NPs, confirming the homogeneous elemental mixing (Figure S1). We also analyzed the crystal structure of the PtPdFeCo NPs at room temperature using atomic HAADF-STEM (Figures 2a and S2a). The d spacings of the intersecting planes were 1.90 and 2.24 Å, which matches the typical (002) and (111) planes of the face centered cubic (FCC) metal structure (e.g., FCC-Pt, JCPDS 01-1190), oriented at the [1–10] zone axis, which was also confirmed from the corresponding fast Fourier transform (FFT) analysis (Figure S2b). Additionally, EDS line scan profiles perpendicular to the (002) plane show all the elements are uniformly distributed (Figure 2b). These results confirmed the successful synthesis of single-phase FCC solid-solution PtPdFeCo-MEA NPs.

To investigate the evolution of the PtPdFeCo NPs in response to elevated temperatures, we heated the NPs to 973 K and held at this temperature for 30 min. After heating, HAADF-STEM imaging revealed an ordered crystal structure within the particle, as demonstrated by the alternating arrangement of bright and dark atomic columns in the images (Figures 2c and S3a). As HAADF imaging is based on atomic number (Z) contrast,[53] the results suggest an ordering of heavy and light atoms may have taken place in this newly formed structure after heating. The d spacings of the two intersecting planes (marked as yellow lines in Figure 2c) in the newly formed structure were 3.80 and 2.22 Å, which matches the distances of the (001) and (111) planes of a typical binary noble-transition metal intermetallic phase structure (e.g., intermetallic PtFe, JCPDS 26-1139). FFT analysis also shows the existence of superlattice spots indicative of (001) and (110) planes (Figure S3b), suggesting the formation of an intermetallic compound. This hypothesis was confirmed by the corresponding elemental maps (Figure 2c) and the intensity line profiles (Figure 2d) perpendicular to the (001) planes (red arrow direction shown in Figure 2c), where an alternating arrangement of Pt–Pd rich and Fe–Co rich atomic columns can be clearly distinguished, as highlighted by the red and green dashed boxes in Figure 2d, respectively. Thus, we can conclude that a quaternary (PtPd)(FeCo) intermetallic $L1_0$ structure was formed after the 973 K-30 min heat treatment.

Interestingly, when we further heated this quaternary intermetallic compound at 1073 K for 30 min, we observed a continuing phase transition phenomenon, in which the

https://doi.org/10.1021/acsnano.5c02343
ACS Nano 2025, 19, 13457–13465

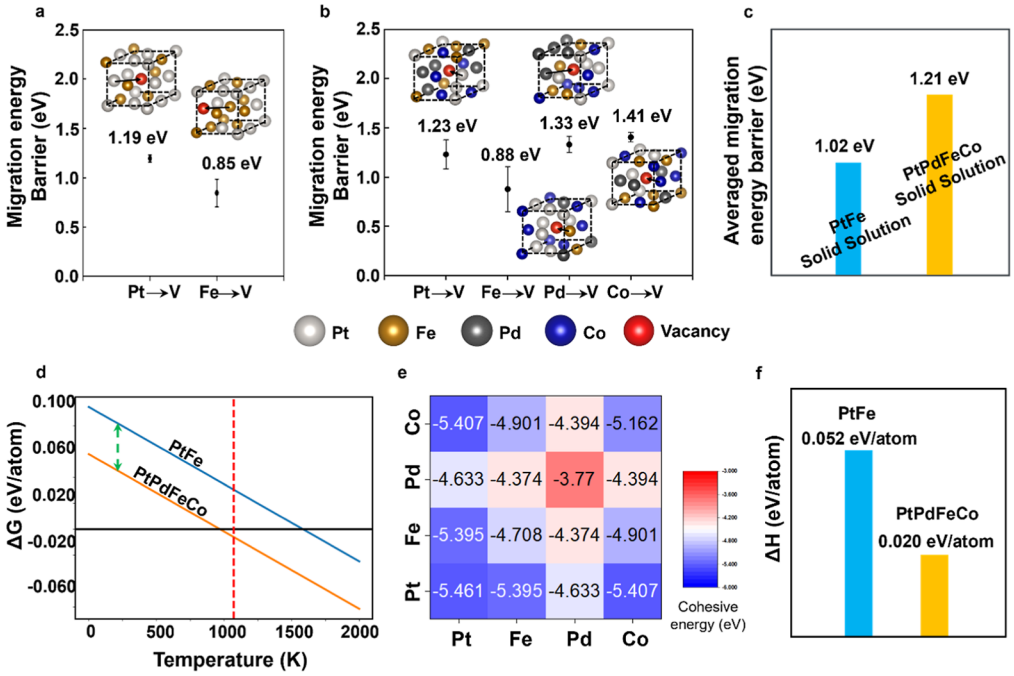

Figure 4. DFT-predicted vacancy migration energies in the (a) PtFe solid solution and (b) PtPdFeCo solid solution. (c) Averaged elemental migration energy in the PtFe and PtPdFeCo solid solution systems. (d) The DFT-predicted Gibbs free energy change (ΔG) for the $L1_0$ intermetallic to solid solution transition in the PtFe and PtPdFeCo alloys. (e) The DFT calculated bonding energies of element pairs between Pt, Pd, Fe, and Co. (f) The bonding energy change (ΔE) of the PtFe and PtPdFeCo system.

intermetallic crystal structure transformed back to a solid solution. As demonstrated by HAADF-STEM (Figure 2e), after heating, we no longer observe periodic contrast in the atomic columns, as evidenced by both the intensity line profile (Figure 2f) and the disappearance of the intermetallic superlattice spots from the FFT analysis (Figure S4). Additionally, the EDS maps and line scans indicate uniform distribution of the Pt, Pd, Fe and Co elements (Figure 2e,f). X-ray diffraction (XRD) analysis after similar heat treatments was conducted on the PtPdFeCo samples as well (Figure S5), demonstrating good consistency with the STEM observations. These results indicate that the PtPdFeCo alloy displays a series of phase evolutions between solid solution and intermetallic, which can be initiated at elevated temperatures.

To better understand this phase transformation, we further explored the transition between the solid solution and intermetallic structures of the PtPdFeCo by heating the pristine PtPdFeCo-MEA NPs at 973 K for just 15 min. HAADF-STEM imaging of the resulting PtPdFeCo alloy shows the atomic arrangement undergoes significant change (Figures 3a and S6). In contrast to the closely packed solid-solution FCC phase at room temperature (Figure 2a), which displayed a distance of ~1.90 Å between the (002) planes, after heating at 973 K for 15 min, neighboring pairs of (002) planes contract to a distance of ~1.61 Å, leaving an increased gap of ~2.19 Å between each pair. To elucidate the underlying elemental migrations that drive the observed change in the crystal structure, we conducted atomic STEM-EDS mapping of the sample (Figure 3a). From these results, we observed a shift of neighboring Pt−Pt and Fe−Fe atoms that take place along the (111) planes, resulting in the formation of closely paired Pt or Fe atoms along with increased gaps between these pairs, as indicated by the white circles and arrows in the Pt and Fe maps. In contrast, the Pd and Co atoms exhibit less migration after the 973 K-15 min heat treatment compared with Pt and Fe.

These elemental migrations drive the process of converting from a solid solution to intermetallic structure, the full evolution of which we explored in the EDS line profiles along the (111) planes of the PtPdFeCo alloy at RT (Figure 3b), and after heating at 973 K for 15 min (Figure 3c) and 30 min (Figure 3d). In the RT solid-solution structure, the distances between neighboring elements are uniformly spaced ~2.32 Å apart along the (111) planes (Figure 3b). After the 973 K-15 min treatment, the distance between adjacent Fe atoms decreased to ~1.58 Å along the (111) planes, with an increased gap distance of ~2.96 Å between the columns of atomic pairs, representing a change of ~30% from the original distances (Figure 3c). Meanwhile, the spacing between Pt atoms was measured to be ~1.97 Å, with a ~2.66 Å gap between the atomic pairs, representing a shift of ~15% from their initial distances, which may be due to the presence of all the elemental atoms in both solid solution and intermetallic structures. As a result of these gradual changes, the Pt and Pd signals align into one sublattice, while the Fe and Co align into a separate sublattice, eventually resulting in a (PtPd)(FeCo) intermetallic structure, as demonstrated in the EDS line scan profile along the (111) plane for the 973 K-30 min treated sample (Figure 3d), in which the elements are ordered into periodic Pt−Pd and Fe−Co sublattice sites, with a distance of ~4.64 Å between the intermetallic sublattice sites.

For comparison, we also prepared binary PtFe solid solution alloy NPs (Figure S7), which have been shown to have a high-temperature ordering transformation.[54,55] These NPs were treated under the same elevated temperatures (973 and 1073 K) for structural and elemental analysis. As shown in Figure S8a, HAADF-STEM imaging shows that the PtFe NPs feature an FCC structure, with both Pt and Fe uniformly distributed across the crystal, as confirmed by the STEM-EDS mapping. After

https://doi.org/10.1021/acsnano.5c02343
ACS Nano 2025, 19, 13457−13465

heating at 973 K for 10 min, the solid solution structure quickly converts to an ordered intermetallic phase, with the Pt and Fe atoms alternatively occupying adjacent atomic columns, as shown by the alternating arrangement of bright and dark dots in the Z contrasted HAADF-STEM imaging (Figure S8b). Thus, the binary PtFe undergoes a solid solution to intermetallic phase transition more readily than the PtPdFeCo-MEA, likely due to the inherent sluggish diffusion effect in MEAs that decreases the overall atomic mobility in the system.[56,57] Additionally, we found the intermetallic PtFe structure was maintained after prolonged heating at 1073 K for 55 min (Figure S8c), with no subsequent phase transition observed.

We performed first-principles density functional theory (DFT) calculations to gain further understanding of these experimentally observed transitions. Specifically, we aimed to explore the different elemental migration trends in the quaternary PtPdFeCo alloy during the phase transitions, as well as to understand why the PtPdFeCo alloy undergoes a series of phase transformations, from solid solution to intermetallic and back to solid solution, whereas the binary PtFe alloy exhibits only a one-way transition from solid solution to intermetallic structure under prolonged heating.

The crystal structures of the disordered and ordered PtFe and PtPdFeCo were constructed through DFT (Figure S9). We calculated the d spacings of (002) and (111) in the PtPdFeCo solid solution to be 1.88 and 2.19 Å, respectively. Similarly, the calculated interplanar spacings for the (001) and (111) planes in $L1_0$ PtPdFeCo were 3.76 and 2.19 Å, respectively (see DFT Methods in the Supporting Information), which well matches the experimental STEM analysis. As we observed experimentally, the thermo-equilibrium at 973 K for both alloys favors the formation of $L1_0$ intermetallic phases, though the process occurs faster for the PtFe sample (10 min heating vs 30 min heating for PtPdFeCo), suggesting that kinetics plays a dominant role over thermodynamics in this disorder-to-order transition process. As atomic migration is believed to occur through the vacancy-exchange mechanism,[54] we calculated the vacancy formation and migration energies of the metal elements through vacancy-assisted diffusion in the PtPdFeCo and PtFe solid solutions using the nudged elastic band (NEB) method.[58] The predicted vacancy formation energies of Pt (1.75 ± 0.25 eV and 1.72 ± 0.13 eV) and Fe (1.39 ± 0.12 eV and 1.49 ± 0.11 eV) in the PtFe and PtPdFeCo alloys, respectively, are similar, with average energies of 1.55 eV for PtFe and 1.57 eV for PtPdFeCo (Figure S10), suggesting that the vacancy concentrations in these alloys should be comparable. Thus, vacancy formation energy is unlikely to be the main factor influencing the transformation from solid solution to intermetallic in these alloys.

Therefore, we next calculated the migration energy for each metal atom along three different diffusion pathways considering the varied local chemical environments. In the PtFe solid solution, the predicted migration energies were 1.19 ± 0.04 eV for Pt and 0.85 ± 0.03 eV for Fe toward adjacent vacancies (Figure 4a). For the PtPdFeCo solid solution, the migration energies of each atom for moving to an adjacent vacancy were predicted to be 1.23 ± 0.15 eV for Pt, 0.88 ± 0.23 eV for Fe, 1.33 ± 0.08 eV for Pd, and 1.41 ± 0.05 eV for Co (Figure 4b). Although the migration energies of Pt and Fe are similar in both systems, the average migration energy in the PtPdFeCo solid solution was 1.21 eV, which is 0.19 eV higher than that in the PtFe solid solution (1.02 eV) (Figure 4c). Thus, the metal atoms should diffuse more slowly in the PtPdFeCo solid solution compared to PtFe. This result agrees well with our experiments, in which the PtPdFeCo solid solution required heating at 973 K for 30 min and the PtFe solid solution for just 10 min to transition from a disordered solid solution to an ordered intermetallic phase. Meanwhile, the DFT results also indicate that the migration energy barrier is lowest for the Fe atoms, followed by Pt, suggesting that Fe and Pt migrate faster than other elements in the PtPdFeCo solid solution, thereby enabling their formation of the two intermetallic sublattice sites more rapidly.

In contrast, the higher migration energies of the Pd and Co atoms make it relatively more difficult for them to diffuse within the system, resulting in slower ordering of Pd and Co into the intermetallic sublattices. These predictions are consistent with our experimental observations that Pt and Fe moved more significantly than Pd and Co from the EDS line profile analysis (Figure 3c). We also hypothesize the material specifically forms (PtPd) and (FeCo) intermetallic sublattices due to the atomic radii of the atoms, as the atom size difference could potentially trigger the phase reconstruction,[59−61] in which Pt and Pd are more similar (1.40 and 1.39 Å), while the size of Fe and Co are closer (1.29 and 1.25 Å) (Table S1).

After further heating to 1073 K, the binary PtFe alloy remains intermetallic, while the quaternary (PtPd)(FeCo) intermetallic transitions back to a solid solution structure. Thus, we explored the thermodynamic driving forces of this intermetallic to solid solution transition.[62] Figure 4d shows the calculated free energy change (ΔG) for the order-to−disorder transition in the PtPdFeCo and PtFe alloys as a function of temperature

$$\Delta G = \Delta H - T\Delta S \tag{1}$$

in which ΔH is the enthalpy change and ΔS is the configurational entropy change from the ordered structure to disordered solid solution, and T is the temperature.

ΔS was calculated to be $R\ln(2)$ for both alloy systems (R is the gas constant, Supporting Information Note SI). Meanwhile, ΔH of this transition was calculated to be 0.058 eV for PtPdFeCo and 0.095 eV for PtFe (Supporting Information Note SII). Therefore, at 1073 K, ΔG for the ordered-to-disordered transition in the PtFePdCo alloy is slightly negative (−0.006 eV/atom), indicating a spontaneous transition toward solid solution would occur, whereas ΔG for the ordered-to-disordered transition in PtFe is significantly more positive (0.031 eV/atom), suggesting less favorability for this transition (Figure S11 and Note SIII). Furthermore, we also performed Monte Carlo (MC) simulations to study the phase transitions of the PtPdFeCo system at elevated temperatures, which show good agreement with our experiments and DFT predictions (Supporting Information Note SVI).

Given that ΔS is the same for both systems, the difference in ΔG is due to enthalpy alone, with ΔH_{PtFe} 0.037 eV/atom higher than $\Delta H_{\mathrm{PtPdFeCo}}$. Generally, the difference in atomic radii and bonding energy are believed to be the two primary factors determining the enthalpy change from an intermetallic to a solid solution phase in an alloy.[63−65] As the phase transitions are mainly a bond reconstruction process, we therefore first performed DFT calculations in terms of the bonding energies of the binary elemental pairs to explore the underlying mechanisms for the difference in ΔH of these two alloys. Based on the calculated bonding energies of the bonded elemental pairs (Figure 4e), and the nearest elemental coordination of all elements in the PtFe and PtPdFeCo systems (Figure S12), the bonding energy change (ΔE) for the transition from intermetallic to solid solution is estimated to be ∼0.052

https://doi.org/10.1021/acsnano.5c02343
ACS Nano 2025, 19, 13457−13465

eV/atom for PtFe, and ∼0.020 eV/atom for PtFePdCo (Figures 4f and Note SIV), resulting in an energy difference of ∼0.032 eV/atom, close to the ΔH difference of 0.037 eV/atom in these two systems. We also take into account the atomic radii difference of all the elements, which appear to have a limited effect on the enthalpy change of the systems during phase transition (Supporting Information Note SV). Thus, we believe it is the bonding energies of the binary bond pairs that play a significant role in determining the differences in ΔH between the PtFe and PtPdFeCo systems, which ultimately governs their phase structures. Overall, our DFT studies unveiled the full spectrum of the two-phase transitions, suggesting that the initial transition from solid solution to intermetallic relies heavily on the migration energies of the elements, while the later intermetallic back to solid solution transition depends more on the bonding energies of all constituents in the alloys. With this information, we also estimated the change in bonding energy for the transition from intermetallic to solid solution phases in PtNi, PtPdFeNi, and PdAuFeCo (Supporting Information Note SVIII).

CONCLUSIONS

In this work, we demonstrate the phase transformations of "disorder-to-order-to-disorder" in quaternary MEA-PtPdFeCo NPs at elevated temperatures through atomic scale crystal structure and elemental distribution analyses. In contrast, the binary PtFe alloy features a simple one-way disorder-to-order transition upon heating. Through atomically precise characterization, we uncovered the relationship between the changing phase structures with the specific elemental arrangements taking place. DFT studies also provide insights from both kinetic and thermodynamic perspectives to elucidate the phase transitions in the quaternary PtPdFeCo and binary PtFe systems at elevated temperatures. Specifically, the initial solid solution to $L1_0$ intermetallic transition in both alloys is governed by the migration energies of the metal elements. The higher average migration energy in the quaternary PtPdFeCo system leads to a slower disorder-to-order transition compared to the binary PtFe. However, in the subsequent transformation from $L1_0$ intermetallic back to solid solution, the lower bonding energies of the quaternary intermetallic lead to a smaller ΔH than in the binary intermetallic, resulting in a disorder-to-order transition at 1073 K. This crystal structure and chemical analysis along with theoretical studies provide a comprehensive understanding of the thermal transformations of this noble-metal-based MEA at the atomic scale, distinguishing between the evolution of the atomic structure and the behavior of individual elements, which could shed light on the design and optimization of MEA catalysts based on composition and phase structure. Future comprehensive studies on the thermal evolution of complex MEA systems, such as high entropy alloys, are worth conducting with well-designed heating and cooling cycles, enabling deeper insights into both the structural and chemical phase changes. Our findings also suggest that when utilizing MEA NPs in high-temperature applications (e.g., thermal catalysis), there may be an intermetallic zone that could cause performance variation during operation. These results can help provide valuable guidance for the design, synthesis, and utilization of MEAs in advanced high-temperature applications.

METHODS

Materials Preparation. Chloroplatinic acid hexahydrate ($H_2PtCl_6{\cdot}xH_2O$), palladium chloride ($PdCl_2$), iron(III) chloride hexahydrate ($FeCl_3{\cdot}6H_2O$), and Cobalt(II) chloride hexahydrate ($CoCl_2{\cdot}6H_2O$), were purchased from Sigma-Aldrich. The metal salts were solubilized in ethanol to form solutions with a metallic ion concentration of 0.05 mol/L. The solutions of $H_2PtCl_6{\cdot}xH_2O$, $PdCl_2$, $FeCl_3{\cdot}6H_2O$, and $CoCl_2{\cdot}6H_2O$ were mixed in equimolar proportions to synthesize the quaternary PtPdFeCo sample, while equimolar $H_2PtCl_6{\cdot}xH_2O$ and $FeCl_3{\cdot}6H_2O$ were mixed to synthesize the binary PtFe sample (see Supporting Information for more details).

STEM Analysis. STEM studies were performed on a JEOL NEOARM operated at 200 kV. The HAADF-STEM images were acquired with a 28 mrad convergence semi-angle. STEM-EDS maps were acquired through JEOL double dry SD 100 GV detectors with a probe current of 120 pA. In situ heating studies were conducted using a Protochips Fusion holder inside the microscope.

Theoretical Calculations. The first-principles calculations were performed using the Vienna ab initio simulation package (VASP) with projector augmented wave (PAW) pseudopotentials. The generalized gradient approximation (GGA) with the Perdew−Burke−Ernzerhof (PBE) exchange−correlation functional was used to evaluate the exchange−correlation energy. In all calculations, the total energy of the system was converged within 10^{-6} eV. A Monkhorst−Pack k-point grid of $4 \times 4 \times 2$ was used. All the structures were fully relaxed until the force acting on each atom was lower than 0.01 eV/Å. The transition states of vacancy migration were located using the nudged elastic band (NEB) method, in which the forces perpendicular to the path were relaxed to less than 0.05 eV/Å. Each NEB calculation included five intermediate images, and migration energy was calculated as the energy difference between the transition state and the initial state.

ASSOCIATED CONTENT

Supporting Information

The Supporting Information is available free of charge at https://pubs.acs.org/doi/10.1021/acsnano.5c02343.

Experimental methods, additional HAADF-STEM images, STEM-EDS line scans and mappings, FFT analysis, theoretical modeling and calculation (PDF)

AUTHOR INFORMATION

Corresponding Authors

Guofeng Wang − *Department of Mechanical Engineering and Materials Science, University of Pittsburgh, Pittsburgh, Pennsylvania 15261, United States;* orcid.org/0000-0001-8249-4101; Email: guw8@pitt.edu

Miaofang Chi − *Center for Nanophase Materials Science, Oak Ridge National Laboratory, Oak Ridge, Tennessee 37831, United States; Thomas Lord Department of Mechanical Engineering and Materials Science, Duke University, Durham, North Carolina 27708, United States;* orcid.org/0000-0003-0764-1567; Email: chim@ornl.gov

Liangbing Hu − *Department of Materials Science and Engineering, University of Maryland, College Park, Maryland 20742, United States; Department of Electrical and Computer Engineering, Yale University, New Haven, Connecticut 06511, United States; Department of Materials Science and Center for Materials Innovation, Yale University, New Haven, Connecticut 06511, United States;* orcid.org/0000-0002-9456-9315; Email: liangbing.hu@yale.edu

Authors

Zhennan Huang − *Department of Materials Science and Engineering, University of Maryland, College Park, Maryland 20742, United States*

Tangyuan Li − *Department of Materials Science and Engineering, University of Maryland, College Park, Maryland 20742, United States; Department of Electrical and Computer*

https://doi.org/10.1021/acsnano.5c02343
ACS Nano 2025, 19, 13457−13465

Engineering, Yale University, New Haven, Connecticut 06511, United States; orcid.org/0009-0001-1232-0613
Ying Fang − *Department of Mechanical Engineering and Materials Science, University of Pittsburgh, Pittsburgh, Pennsylvania 15261, United States*
Jacob Smith − *Center for Nanophase Materials Science, Oak Ridge National Laboratory, Oak Ridge, Tennessee 37831, United States*
Boyang Li − *Department of Mechanical Engineering and Materials Science, University of Pittsburgh, Pittsburgh, Pennsylvania 15261, United States*
Alexandra Brozena − *Department of Materials Science and Engineering, University of Maryland, College Park, Maryland 20742, United States; Department of Electrical and Computer Engineering, Yale University, New Haven, Connecticut 06511, United States*
Qi Dong − *Department of Materials Science and Engineering, University of Maryland, College Park, Maryland 20742, United States;* orcid.org/0000-0002-7553-4213
Qian Zhang − *Department of Materials Science and Engineering, University of Maryland, College Park, Maryland 20742, United States; Department of Electrical and Computer Engineering, Yale University, New Haven, Connecticut 06511, United States*
Yiheng Du − *Department of Materials Science and Engineering, University of Maryland, College Park, Maryland 20742, United States; Department of Electrical and Computer Engineering, Yale University, New Haven, Connecticut 06511, United States*
Scott X. Mao − *Department of Mechanical Engineering and Materials Science, University of Pittsburgh, Pittsburgh, Pennsylvania 15261, United States*

Complete contact information is available at:
https://pubs.acs.org/10.1021/acsnano.5c02343

Author Contributions

[▽]Z.H., T.L. and Y.F. contributed equally to this work. Z.H. and L.H. designed the research; Z.H., J.S. and M.C. performed the TEM studies and data interpretation; T.L., Q.D., Q.Z. and Y.D. performed the materials synthesis and XRD characterizations. Y.F., B.L., S.M. and G.W. contributed on the DFT; Z.H., A.B., Y.F., G.W. and L.H. wrote the paper. All authors were involved in the discussion of the manuscript and provided meaningful comments.

Notes

The authors declare no competing financial interest.

ACKNOWLEDGMENTS

Z.H. and L.H. would like to acknowledge the supported by the U.S. Department of Energy (DOE), Office of Science, Office of Basic Energy Sciences (BES), CSGB Division under Award no. DE-SC0023357, and also acknowledge the financial support from the U.S. Department of Energy, Office of Science Energy Earthshot Initiative as part of the Non-equilibrium Energy Transfer for Efficient Reactions (NEETER) at Oak Ridge National Laboratory under contract no. DE-AC05-00OR22725. Part of the Research was sponsored by the U.S. DOE, Office of Science, Office of Basic Energy Sciences (BES), Chemical Sciences, Geosciences, and Biosciences Division, Catalysis Science program. M.C. would like to thank the support by the U.S. Department of Energy, Office of Science, Basic Energy Sciences, Materials Sciences, and Engineering Division. Technique development and data analysis were supported by U.S. DOE Office of Science under Early Career award no. ERKCZ55. Microscopy experiments were performed at the Center for Nanophase Materials Sciences (CNMS), which is a US Department of Energy, Office of Science User Facility at Oak Ridge National Laboratory. Y.F. and G.W. acknowledge the support from National Science Foundation (NSF-CMMI 1760916) through the University of Pittsburgh. This research was supported in part by the University of Pittsburgh Center for Research Computing through the resources provided. Specifically, this work used the H2P cluster, which is supported by NSF award number OAC-2117681.

REFERENCES

(1) Yao, Y.; Huang, Z.; Xie, P.; Lacey, S. D.; Jacob, R. J.; Xie, H.; Chen, F.; Nie, A.; Pu, T.; Rehwoldt, M.; Yu, D.; Zachariah, M. R.; Wang, C.; Shahbazian-Yassar, R.; Li, J.; Hu, L. Carbothermal Shock Synthesis of High-Entropy-Alloy Nanoparticles. *Science* **2018**, *359* (6383), 1489−1494.
(2) Sun, Y.; Dai, S. High-Entropy Materials for Catalysis: A New Frontier. *Sci. Adv.* **2021**, *7* (20), 1−24.
(3) Cao, G.; Liang, J.; Guo, Z.; Yang, K.; Wang, G.; Wang, H.; Wan, X.; Li, Z.; Bai, Y.; Zhang, Y.; Liu, J.; Feng, Y.; Zheng, Z.; Lu, C.; He, G.; Xiong, Z.; Liu, Z.; Chen, S.; Guo, Y.; Zeng, M.; Lin, J.; Fu, L. Liquid Metal for High-Entropy Alloy Nanoparticles Synthesis. *Nature* **2023**, *619* (7968), 73−77.
(4) Sun, Y.; Dai, S. Synthesis of High-Entropy Materials. *Nat., Synth.* **2024**, *3* (12), 1457−1470.
(5) Yoosefan, F.; Ashrafi, A.; Monir Vaghefi, S. M. Corrosion and Tribological Behavior of CoCrFeMoNi High-Entropy Alloys as a Potential Vascular Implant Material. *J. Alloys Compd.* **2024**, *976*, 172964.
(6) Wang, X.; Bai, W.; Zhang, Z.; Wang, Z.; Ren, X. Enhanced Fatigue Resistance of a Face-Centered-Cubic Single-Phase Al0.3CoCrFeNi High-Entropy Alloy through Planar Deformation Characteristic. *Mater. Sci. Eng. A* **2023**, *862*, 144499.
(7) San, S.; Adhikari, P.; Sakidja, R.; Brechtl, J.; Liaw, P. K.; Ching, W.-Y. Porosity Modeling in a TiNbTaZrMo High-Entropy Alloy for Biomedical Applications. *RSC Adv.* **2023**, *13* (51), 36468−36476.
(8) Löffler, T.; Savan, A.; Garzón-Manjón, A.; Meischein, M.; Scheu, C.; Ludwig, A.; Schuhmann, W. Toward a Paradigm Shift in Electrocatalysis Using Complex Solid Solution Nanoparticles. *ACS Energy Lett.* **2019**, *4* (5), 1206−1214.
(9) Xie, P.; Yao, Y.; Huang, Z.; Liu, Z.; Zhang, J.; Li, T.; Wang, G.; Shahbazian-Yassar, R.; Hu, L.; Wang, C. Highly Efficient Decomposition of Ammonia Using High-Entropy Alloy Catalysts. *Nat. Commun.* **2019**, *10* (1), 4011.
(10) Pedersen, J. K.; Batchelor, T. A. A.; Bagger, A.; Rossmeisl, J. High-Entropy Alloys as Catalysts for the Co2 and Co Reduction Reactions. *ACS Catal.* **2020**, *10* (3), 2169−2176.
(11) Yao, Y.; Liu, Z.; Xie, P.; Huang, Z.; Li, T.; Morris, D.; Finfrock, Z.; Zhou, J.; Jiao, M.; Gao, J.; et al. Computationally aided, entropy-driven synthesis of highly efficient and durable multi-elemental alloy catalysts. *Sci. Adv.* **2020**, *6* (11), No. eaaz0510.
(12) Marques, F.; Balcerzak, M.; Winkelmann, F.; Zepon, G.; Felderhoff, M. Review and Outlook on High-Entropy Alloys for Hydrogen Storage. *Energy Environ. Sci.* **2021**, *14* (10), 5191−5227.
(13) Zlotea, C.; Bouzidi, A.; Montero, J.; Ek, G.; Sahlberg, M. Compositional Effects on the Hydrogen Storage Properties in a Series of Refractory High Entropy Alloys. *Front. Energy Res.* **2022**, *10*, 991447.
(14) Moore, C. M.; Wilson, J. A.; Rushton, M. J. D.; Lee, W. E.; Astbury, J. O.; Middleburgh, S. C. Hydrogen Accommodation in the TiZrNbHfTa High Entropy Alloy. *Acta Mater.* **2022**, *229*, 117832.
(15) Banko, L.; Krysiak, O. A.; Pedersen, J. K.; Xiao, B.; Savan, A.; Löffler, T.; Baha, S.; Rossmeisl, J.; Schuhmann, W.; Ludwig, A. Unravelling Composition−Activity−Stability Trends in High Entropy Alloy Electrocatalysts by Using a Data-Guided Combinatorial Synthesis

Strategy and Computational Modeling. *Adv. Energy Mater.* **2022**, *12* (8), 2103312.
(16) Yao, Y.; Huang, Z.; Hughes, L. A.; Gao, J.; Li, T.; Morris, D.; Zeltmann, S. E.; Savitzky, B. H.; Ophus, C.; Finfrock, Y. Z.; et al. Extreme mixing in nanoscale transition metal alloys. *Matter* **2021**, *4* (7), 2340−2353.
(17) Löffler, T.; Savan, A.; Meyer, H.; Meischein, M.; Strotkötter, V.; Ludwig, A.; Schuhmann, W. Design of Complex Solid-Solution Electrocatalysts by Correlating Configuration, Adsorption Energy Distribution Patterns, and Activity Curves. *Angew. Chem. Int. Ed.* **2020**, *59* (14), 5844−5850.
(18) Banko, L.; Tetteh, E. B.; Kostka, A.; Piotrowiak, T. H.; Krysiak, O. A.; Hagemann, U.; Andronescu, C.; Schuhmann, W.; Ludwig, A. Microscale Combinatorial Libraries for the Discovery of High-Entropy Materials. *Adv. Mater.* **2023**, *35* (9), 2207635.
(19) Zhang, Y.; Wang, D.; Wang, S. High-Entropy Alloys for Electrocatalysis: Design, Characterization, and Applications. *Small* **2022**, *18* (7), 1−22.
(20) Shi, Y.; Yang, B.; Liaw, P. K. Corrosion-Resistant High-Entropy Alloys: A Review. *Metals* **2017**, *7* (2), 43.
(21) Gludovatz, B.; Hohenwarter, A.; Catoor, D.; Chang, E. H.; George, E. P.; Ritchie, R. O. A Fracture-Resistant High-Entropy Alloy for Cryogenic Applications. *Science* **2014**, *345* (6201), 1153−1158.
(22) Yao, Y.; Huang, Z.; Li, T.; Wang, H.; Liu, Y.; Stein, H. S.; Mao, Y.; Gao, J.; Jiao, M.; Dong, Q.; et al. High-throughput, combinatorial synthesis of multimetallic nanoclusters. *Proc. Natl. Acad. Sci. U.S.A.* **2020**, *117* (12), 6316−6322.
(23) Reddy, T. S.; Wani, I. S.; Bhattacharjee, T.; Reddy, S. R.; Saha, R.; Bhattacharjee, P. P. Severe Plastic Deformation Driven Nanostructure and Phase Evolution in a Al 0.5 CoCrFeMnNi Dual Phase High Entropy Alloy. *Intermetallics* **2017**, *91*, 150−157.
(24) MacDonald, B. E.; Fu, Z.; Wang, X.; Li, Z.; Chen, W.; Zhou, Y.; Raabe, D.; Schoenung, J.; Hahn, H.; Lavernia, E. J. Influence of Phase Decomposition on Mechanical Behavior of an Equiatomic CoCuFeMnNi High Entropy Alloy. *Acta Mater.* **2019**, *181*, 25−35.
(25) Chen, S.; Aitken, Z. H.; Pattamatta, S.; Wu, Z.; Yu, Z. G.; Srolovitz, D. J.; Liaw, P. K.; Zhang, Y.-W. Simultaneously Enhancing the Ultimate Strength and Ductility of High-Entropy Alloys via Short-Range Ordering. *Nat. Commun.* **2021**, *12* (1), 4953.
(26) Cui, M.; Yang, C.; Hwang, S.; Yang, M.; Overa, S.; Dong, Q.; Yao, Y.; Brozena, A. H.; Cullen, D. A.; Chi, M.; Blum, T. F.; Morris, D.; Finfrock, Z.; Wang, X.; Zhang, P.; Goncharov, V. G.; Guo, X.; Luo, J.; Mo, Y.; Jiao, F.; Hu, L. Multi-Principal Elemental Intermetallic Nanoparticles Synthesized via a Disorder-to-Order Transition. *Sci. Adv.* **2022**, *8* (4), No. eabm4322.
(27) Chen, S. Y.; Tong, Y.; Tseng, K.-K.; Yeh, J.-W.; Poplawsky, J. D.; Wen, J. G.; Gao, M. C.; Kim, G.; Chen, W.; Ren, Y.; Feng, R.; Li, W. D.; Liaw, P. K. Phase Transformations of HfNbTaTiZr High-Entropy Alloy at Intermediate Temperatures. *Scr. Mater.* **2019**, *158*, 50−56.
(28) Du, J. P.; Yu, P.; Shinzato, S.; Meng, F. S.; Sato, Y.; Li, Y.; Fan, Y.; Ogata, S. Chemical Domain Structure and Its Formation Kinetics in CrCoNi Medium-Entropy Alloy. *Acta Mater.* **2022**, *240*, 118314.
(29) Yang, C.-L.; Wang, L.-N.; Yin, P.; Liu, J.; Chen, M.-X.; Yan, Q.-Q.; Wang, Z.-S.; Xu, S.-L.; Chu, S.-Q.; Cui, C.; Ju, H.; Zhu, J.; Lin, Y.; Shui, J.; Liang, H.-W. Sulfur-Anchoring Synthesis of Platinum Intermetallic Nanoparticle Catalysts for Fuel Cells. *Science* **2021**, *374* (6566), 459−464.
(30) Chen, T.; Qiu, C.; Zhang, X.; Wang, H.; Song, J.; Zhang, K.; Yang, T.; Zuo, Y.; Yang, Y.; Gao, C.; Xiao, W.; Jiang, Z.; Wang, Y.; Xiang, Y.; Xia, D. An Ultrasmall Ordered High-Entropy Intermetallic with Multiple Active Sites for the Oxygen Reduction Reaction. *J. Am. Chem. Soc.* **2024**, *146*, 1174.
(31) Xin, Y.; Li, S.; Qian, Y.; Zhu, W.; Yuan, H.; Jiang, P.; Guo, R.; Wang, L. High-Entropy Alloys as a Platform for Catalysis: Progress, Challenges, and Opportunities. *ACS Catal.* **2020**, *10* (19), 11280−11306.
(32) Yao, Y.; Liu, Z.; Xie, P.; Huang, Z.; Li, T.; Morris, D.; Finfrock, Z.; Zhou, J.; Jiao, M.; Gao, J.; Mao, Y.; Miao, J.; Zhang, P.; Shahbazian-Yassar, R.; Wang, C.; Wang, G.; Hu, L. Computationally Aided, Entropy-Driven Synthesis of Highly Efficient and Durable Multi-Elemental Alloy Catalysts. *Sci. Adv.* **2020**, *6* (11), No. eaaz0510.
(33) Liu, H.; Zhang, Y.; Zhang, L.; Mu, X.; Zhang, L.; Zhu, S.; Wang, K.; Yu, B.; Jiang, Y.; Zhou, J.; Yang, F. Unveiling Atomic-Scaled Local Chemical Order of High-Entropy Intermetallic Catalyst for Alkyl-Substitution-Dependent Alkyne Semihydrogenation. *J. Am. Chem. Soc.* **2024**, *146* (29), 20193−20204.
(34) Yin, P.; Niu, X.; Li, S.-B.; Chen, K.; Zhang, X.; Zuo, M.; Zhang, L.; Liang, H.-W. Machine-Learning-Accelerated Design of High-Performance Platinum Intermetallic Nanoparticle Fuel Cell Catalysts. *Nat. Commun.* **2024**, *15* (1), 415.
(35) Chen, W.; Luo, S.; Sun, M.; Wu, X.; Zhou, Y.; Liao, Y.; Tang, M.; Fan, X.; Huang, B.; Quan, Z. High-Entropy Intermetallic PtRhBiSnSb Nanoplates for Highly Efficient Alcohol Oxidation Electrocatalysis. *Adv. Mater.* **2022**, *34* (43), 2206276.
(36) Zhang, L.; Zhang, X.; Chen, C.; Zhang, J.; Tan, W.; Xu, Z.; Zhong, Z.; Du, L.; Song, H.; Liao, S.; Zhu, Y.; Zhou, Z.; Cui, Z. Machine Learning-Aided Discovery of Low-Pt High Entropy Intermetallic Compounds for Electrochemical Oxygen Reduction Reaction. *Angew. Chem.* **2024**, *136* (51), No. e202411123.
(37) Lin, F.; Li, M.; Zeng, L.; Luo, M.; Guo, S. Intermetallic Nanocrystals for Fuel-Cells-Based Electrocatalysis. *Chem. Rev.* **2023**, *123* (22), 12507−12593.
(38) Liu, J.; Dong, S.; Gai, S.; Dong, Y.; Liu, B.; Zhao, Z.; Xie, Y.; Feng, L.; Yang, P.; Lin, J. Design and Mechanism Insight of Monodispersed AuCuPt Alloy Nanozyme with Antitumor Activity. *ACS Nano* **2023**, *17* (20), 20402−20423.
(39) Yang, M.; Li, B.; Li, S.; Dong, Q.; Huang, Z.; Zheng, S.; Fang, Y.; Zhou, G.; Chen, X.; Zhu, X.; Li, T.; Chi, M.; Wang, G.; Hu, L.; Ren, Z. J. Highly Selective Electrochemical Nitrate to Ammonia Conversion by Dispersed Ru in a Multielement Alloy Catalyst. *Nano Lett.* **2023**, *23* (16), 7733−7742.
(40) Wu, C.-Y.; Hsiao, Y.-C.; Chen, Y.; Lin, K.-H.; Lee, T.-J.; Chi, C.-C.; Lin, J.-T.; Hsu, L.-C.; Tsai, H.-J.; Gao, J.-Q.; Chang, C.-W.; Kao, I.-T.; Wu, C.-Y.; Lu, Y.-R.; Pao, C.-W.; Hung, S.-F.; Lu, M.-Y.; Zhou, S.; Yang, T.-H. A Catalyst Family of High-Entropy Alloy Atomic Layers with Square Atomic Arrangements Comprising Iron- and Platinum-Group Metals. *Sci. Adv.* **2024**, *10* (30), No. eadl3693.
(41) Jiang, B.; Bridges, C. A.; Unocic, R. R.; Pitike, K. C.; Cooper, V. R.; Zhang, Y.; Lin, D. Y.; Page, K. Probing the Local Site Disorder and Distortion in Pyrochlore High-Entropy Oxides. *J. Am. Chem. Soc.* **2021**, *143* (11), 4193−4204.
(42) Seol, J. B.; Ko, W.-S.; Sohn, S. S.; Na, M. Y.; Chang, H. J.; Heo, Y.-U.; Kim, J. G.; Sung, H.; Li, Z.; Pereloma, E.; Kim, H. S. Mechanically Derived Short-Range Order and Its Impact on the Multi-Principal-Element Alloys. *Nat. Commun.* **2022**, *13* (1), 1−13.
(43) Lei, Z.; Liu, X.; Wu, Y.; Wang, H.; Jiang, S.; Wang, S.; Hui, X.; Wu, Y.; Gault, B.; Kontis, P.; Raabe, D.; Gu, L.; Zhang, Q.; Chen, H.; Wang, H.; Liu, J.; An, K.; Zeng, Q.; Nieh, T. G.; Lu, Z. Enhanced Strength and Ductility in a High-Entropy Alloy via Ordered Oxygen Complexes. *Nature* **2018**, *563* (7732), 546−550.
(44) Ren, J.; Zhang, Y.; Zhao, D.; Chen, Y.; Guan, S.; Liu, Y.; Liu, L.; Peng, S.; Kong, F.; Poplawsky, J. D.; Gao, G.; Voisin, T.; An, K.; Wang, Y. M.; Xie, K. Y.; Zhu, T.; Chen, W. Strong yet Ductile Nanolamellar High-Entropy Alloys by Additive Manufacturing. *Nature* **2022**, *608* (7921), 62−68.
(45) Santodonato, L. J.; Zhang, Y.; Feygenson, M.; Parish, C. M.; Gao, M. C.; Weber, R. J. K.; Neuefeind, J. C.; Tang, Z.; Liaw, P. K. Deviation from High-Entropy Configurations in the Atomic Distributions of a Multi-Principal-Element Alloy. *Nat. Commun.* **2015**, *6*, 5964.
(46) Zhu, M.; Wachs, I. E. Iron-Based Catalysts for the High-Temperature Water−Gas Shift (HT-WGS) Reaction: A Review. *ACS Catal.* **2016**, *6* (2), 722−732.
(47) Liu, L.; Lopez-Haro, M.; Lopes, C. W.; Li, C.; Concepcion, P.; Simonelli, L.; Calvino, J. J.; Corma, A. Regioselective Generation and Reactivity Control of Subnanometric Platinum Clusters in Zeolites for High-Temperature Catalysis. *Nat. Mater.* **2019**, *18* (8), 866−873.

https://doi.org/10.1021/acsnano.5c02343
ACS Nano 2025, 19, 13457−13465

(48) Shroti, N.; Daletou, M. K. The Pt−Co Alloying Effect on the Performance and Stability of High Temperature PEMFC Cathodes. *Int. J. Hydrogen Energy* **2022**, *47* (36), 16235−16248.
(49) Ma, H.; Schneider, W. F. DFT and microkinetic comparison of Pt, Pd and Rh-catalyzed ammonia oxidation. *J. Catal.* **2020**, *383*, 322−330.
(50) Song, T.-W.; Xu, C.; Sheng, Z.-T.; Yan, H.-K.; Tong, L.; Liu, J.; Zeng, W.-J.; Zuo, L.-J.; Yin, P.; Zuo, M.; Chu, S.-Q.; Chen, P.; Liang, H.-W. Small Molecule-Assisted Synthesis of Carbon Supported Platinum Intermetallic Fuel Cell Catalysts. *Nat. Commun.* **2022**, *13* (1), 6521.
(51) Hou, Z.; Lu, Y.; Liu, Y.; Liu, N.; Hu, J.; Wei, L.; Li, Z.; Tian, X.; Gao, R.; Yu, X.; Feng, Y.; Wu, L.; Deng, J.; Wang, D.; Sui, M.; Dai, H.; Li, Y. A General Dual-Metal Nanocrystal Dissociation Strategy to Generate Robust High-Temperature-Stable Alumina-Supported Single-Atom Catalysts. *J. Am. Chem. Soc.* **2023**, *145* (29), 15869−15878.
(52) Han, J.; Yang, J.; Zhang, Z.; Jiang, X.; Liu, W.; Qiao, B.; Mu, J.; Wang, F. Strong Metal−Support Interaction Facilitated Multicomponent Alloy Formation on Metal Oxide Support. *J. Am. Chem. Soc.* **2023**, *145* (41), 22671−22684.
(53) Nellist, P. D.; Pennycook, S. J. The principles and interpretation of annular dark-field Z-contrast imaging. In *The principles and interpretation of annular dark-field Z-contrast imaging*; Elsevier, 2000; Vol. *113*, pp 147−203..
(54) Chen, X.; Zhang, S.; Li, C.; Liu, Z.; Sun, X.; Cheng, S.; Zakharov, D. N.; Hwang, S.; Zhu, Y.; Fang, J.; Wang, G.; Zhou, G. Composition-Dependent Ordering Transformations in Pt−Fe Nanoalloys. *Proc. Natl. Acad. Sci. U.S.A.* **2022**, *119* (14), No. e2117899119.
(55) Gong, M.; Shen, T.; Deng, Z.; Yang, H.; Li, Z.; Zhang, J.; Zhang, R.; Hu, Y.; Zhao, X.; Xin, H.; Wang, D. Surface Engineering of PdFe Ordered Intermetallics for Efficient Oxygen Reduction Electrocatalysis. *Chem. Eng. J.* **2021**, *408*, 127297.
(56) Divinski, S. V.; Pokoev, A. V.; Esakkiraja, N.; Paul, A. A Mystery of "Sluggish Diffusion" in High-Entropy Alloys: The Truth or a Myth? *Diffus. Found.* **2018**, *17*, 69−104.
(57) Miracle, D. B.; Senkov, O. N. A Critical Review of High Entropy Alloys and Related Concepts. *Acta Mater.* **2017**, *122*, 448−511.
(58) Henkelman, G.; Uberuaga, B. P.; Jónsson, H. A Climbing Image Nudged Elastic Band Method for Finding Saddle Points and Minimum Energy Paths. *J. Chem. Phys.* **2000**, *113* (22), 9901−9904.
(59) Zhang, F. X.; Song, H.-Q. Effect of Atomic Size Mismatch and Chemical Complexity on the Local Lattice Distortion of BCC Solid Solution Alloys. *Mater. Today Commun.* **2022**, *33*, 104367.
(60) Wang, H.; He, Q.-F.; Yang, Y. High-Entropy Intermetallics: From Alloy Design to Structural and Functional Properties. *Rare Met.* **2022**, *41* (6), 1989−2001.
(61) Poletti, M. G.; Battezzati, L. Electronic and Thermodynamic Criteria for the Occurrence of High Entropy Alloys in Metallic Systems. *Acta Mater.* **2014**, *75*, 297−306.
(62) Eisenbach, M.; Pei, Z.; Liu, X. First-Principles Study of Order-Disorder Transitions in Multicomponent Solid-Solution Alloys. *J. Phys.: Condens. Matter* **2019**, *31* (27), 273002.
(63) Otto, F.; Yang, Y.; Bei, H.; George, E. P. Relative Effects of Enthalpy and Entropy on the Phase Stability of Equiatomic High-Entropy Alloys. *Acta Mater.* **2013**, *61* (7), 2628−2638.
(64) Uporov, S.; Estemirova, S. Kh.; Bykov, V. A.; Zamyatin, D. A.; Ryltsev, R. E. A Single-Phase ScTiZrHf High-Entropy Alloy with Thermally Stable Hexagonal Close-Packed Structure. *Intermetallics* **2020**, *122*, 106802.
(65) Chen, S.; Aitken, Z. H.; Pattamatta, S.; Wu, Z.; Yu, Z. G.; Banerjee, R.; Srolovitz, D. J.; Liaw, P. K.; Zhang, Y.-W. Chemical-Affinity Disparity and Exclusivity Drive Atomic Segregation, Short-Range Ordering, and Cluster Formation in High-Entropy Alloys. *Acta Mater.* **2021**, *206*, 116638.

https://doi.org/10.1021/acsnano.5c02343
ACS Nano 2025, 19, 13457−13465